Editors' Suggestion

Optical magnetoelectric effects resonantly enhanced via electromagnons in cycloidal helimagnets $Eu_{1-x}Y_xMnO_3$

M. Ogino,[1,*] Y. Kaneko,[2] Y. Tokura,[1,2,3] and Y. Takahashi[1,2,*]

[1]*Quantum-Phase Electronics Center and Department of Applied Physics, The University of Tokyo, Tokyo 113-8656, Japan*

[2]*RIKEN Center for Emergent Matter Science, Wako 351-0198, Japan*

[3]*Tokyo College, The University of Tokyo, Tokyo 113-8656, Japan*

(Received 27 February 2023; accepted 29 June 2023; published 20 July 2023)

We investigate the optical magnetoelectric (ME) effects which lead to the nonreciprocity of photons arising from the enhanced dynamical ME coupling of the electromagnon resonances in the spin-cycloidal phases of multiferroic perovskite manganites $Eu_{1-x}Y_xMnO_3$ ($x = 0.3$, 0.4, 0.45, 0.5) by means of terahertz time-domain polarimetry. The correlation between the optical ME effects and the associated order parameters is examined by changing x. Nonreciprocal directional dichroism (NDD) is demonstrated in the *ab*- and *bc*-plane cycloidal phases. The resonantly enhanced NDD in the *ab*-plane cycloidal phase shows correlation with the relevant coupled order parameter composed of spontaneous polarization $\boldsymbol{P}$ and magnetization $\boldsymbol{M}$ as $\boldsymbol{P} \times \boldsymbol{M}$. The NDD is further enhanced in the *bc*-plane cycloidal phase due to the mode-mode coupling of electromagnons with distinct origins. The nonreciprocal optical rotation stemming from gyrotropic birefringence (GB) is also demonstrated in the *ab*-plane spin cycloidal phase. The magnitude of GB shows clear deviations from the relevant coupled order parameter of $\boldsymbol{P} \cdot \boldsymbol{M}$. The GB is remarkably enhanced near the phase boundary ($x = 0.3$) between the cycloidal phase and the canted antiferromagnetic phase. As a result, the dynamical diagonal ME coupling approaches 0.23 (770 ps/m) for $x = 0.3$. These different x dependences between NDD and the GB are discussed on the basis of the mechanisms of the dynamical ME coupling of collective spin excitations.

DOI: 10.1103/PhysRevB.108.024418

I. INTRODUCTION

Cross-coupling between electric and magnetic properties, i.e., magnetoelectric (ME) coupling, emerges in particular classes of materials, enabling the electric field control of the magnetism and vice versa [1–3]. Multiferroics with spin-driven ferroelectricity exhibit dramatically enhanced ME coupling, as exemplified by the flop of the spontaneous polarization $\boldsymbol{P}$ by the magnetic field [4] and the magnetization $\boldsymbol{M}$ reversal by the electric field [5]. Novel logic and memory devices based on ME coupling with low-energy consumption have been proposed [3,6].

In addition to the responses to the static fields, the dynamical ME coupling appears in response to the electromagnetic field of light, resulting in nonreciprocal optical phenomena [7]: the optical responses change with the reversal of the propagation vector of light $\boldsymbol{k}^{\omega}$. For example, nonreciprocal directional dichroism [NDD; Fig. 1(a)] is observed as the optical diode effect [8–10]; the reversal of $\boldsymbol{k}^{\omega}$ results in a change in the optical absorption while keeping the light polarization intact. The dynamical ME coupling also exhibits the nonreciprocity for light polarization, which is termed gyrotropic birefringence [GB; Fig. 1(b)]. The resulting optical rotation is distinguished from conventional optical rotation phenomena such as the Faraday effect and natural optical activity. Recently, it was demonstrated that the GB can be viewed as the nonreciprocal rotation of the eigenpolarization of crystals [11].

The optical ME effects were initially observed for the ME antiferromagnet Cr_2O_3 [12] and for the molecular liquid in electric and magnetic fields [13,14]. The discovery of ME multiferroics with spin-driven ferroelectricity [1,2,4] accelerated the study of optical ME effects because they enhance the dynamical ME coupling in specific optical transitions. The electromagnon, which is a magnon endowed with electric activity, represents such ME excitation. Since the ferroelectricity in multiferroics of spin origin is induced by some long-range spin orders [15,16], the fluctuation of the spin orders always possesses the electric response (typically in the terahertz region), giving rise to electromagnon resonance [17]. For example, a giant NDD on the electromagnon, which exceeds $\Delta\kappa \sim 1$ in the change in the extinction coefficient κ, was found in the multiferroic perovskite manganite $Gd_{0.5}Tb_{0.5}MnO_3$ [9].

So far the optical ME effects have been studied for individual materials. The systematic research on optical ME effects, which tests the correlation with relevant parameters, provides insight into the mechanism of the dynamical ME coupling and the enhancement of nonreciprocal optical effects. Perovskite manganites $RMnO_3$ (R: rare earth), which are the most archetypal multiferroics of spin origin, are suitable for this systematic research. In $RMnO_3$, the cycloidal spin-spiral order emerges owing to the frustration of spin interactions, which can be controlled by changing the radius of rare earth ions. This cycloidal spin-spiral order breaking the space-inversion

*Corresponding author: youtarou-takahashi@ap.t.u-tokyo.ac.jp

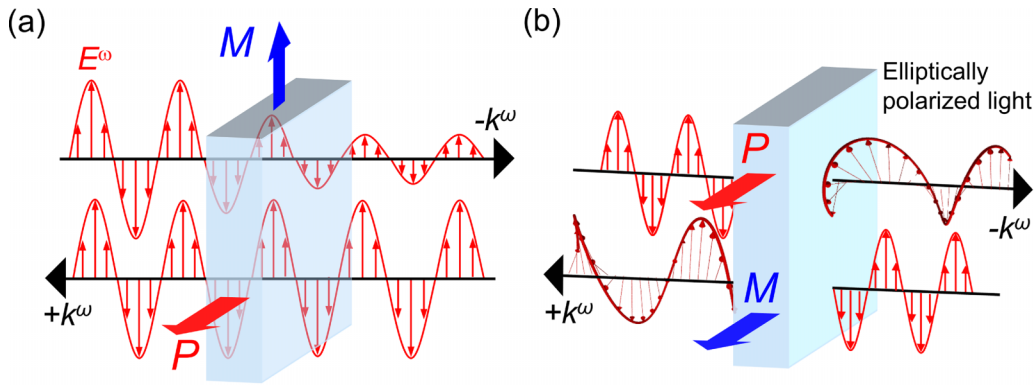

FIG. 1. Schematics of (a) NDD and (b) GB. The materials have both electric polarization $\boldsymbol{P}$ and magnetization $\boldsymbol{M}$; (a) $\boldsymbol{P} \perp \boldsymbol{M}$ for NDD, and (b) $\boldsymbol{P} \parallel \boldsymbol{M}$ for GB. The electric field of light is represented by red arrows (E^ω). Owing to the nonreciprocity of optical ME effects, the optical responses of NDD and GB change with the sign reversal of the propagation vector of light $\boldsymbol{k}^\omega$.

symmetry gives rise to the spin-driven ferroelectricity, which is explained by the inverse Dzyaloshinskii-Moriya (IDM) mechanism [15,16,18]; the spontaneous polarization $\boldsymbol{P}$ is expressed as $\boldsymbol{P} \propto \sum_{ij} \boldsymbol{e}_{ij} \times (\boldsymbol{S}_i \times \boldsymbol{S}_j)$, where $\boldsymbol{e}_{ij}$ is the unit vector connecting the neighboring spin pairs, $\boldsymbol{S}_i$ and $\boldsymbol{S}_j$. The cycloidal spin structures are stabilized either in the *ab* plane [Fig. 2(a)] or in the *bc* plane [Fig. 2(b)] with the magnetic modulation vector along the *b* axis, giving rise to $\boldsymbol{P}$ along the *a* or *c* axis, respectively. Hereafter, we denote these spin structures as the *ab* cycloid ($\boldsymbol{P} \parallel a$) and the *bc* cycloid ($\boldsymbol{P} \parallel c$). The solid solution system $Eu_{1-x}Y_xMnO_3$ provides a magnetic system composed of only the spins on the Mn^{3+} site because of the absence of the magnetic moment on the *f* electrons in Eu^{3+} and Y^{3+}. Between $x = 0.3$ and $x = 0.5$, the ground state is the *ab* cycloid [red area in Fig. 2(c)], while the *bc* cycloid [blue area in Fig. 2(c)] emerges at intermediate temperature and in the magnetic field along the *a* axis, as shown in Fig. 2(c) [22–25]. In the magnetic field along the *c* axis, the spin structure remains the *ab* cycloid below 7 T.

In this paper, we systematically investigate the enhanced optical ME effects, NDD and GB, on the electromagnons in multiferroic perovskite manganites $Eu_{1-x}Y_xMnO_3$ ($x = 0.3$,

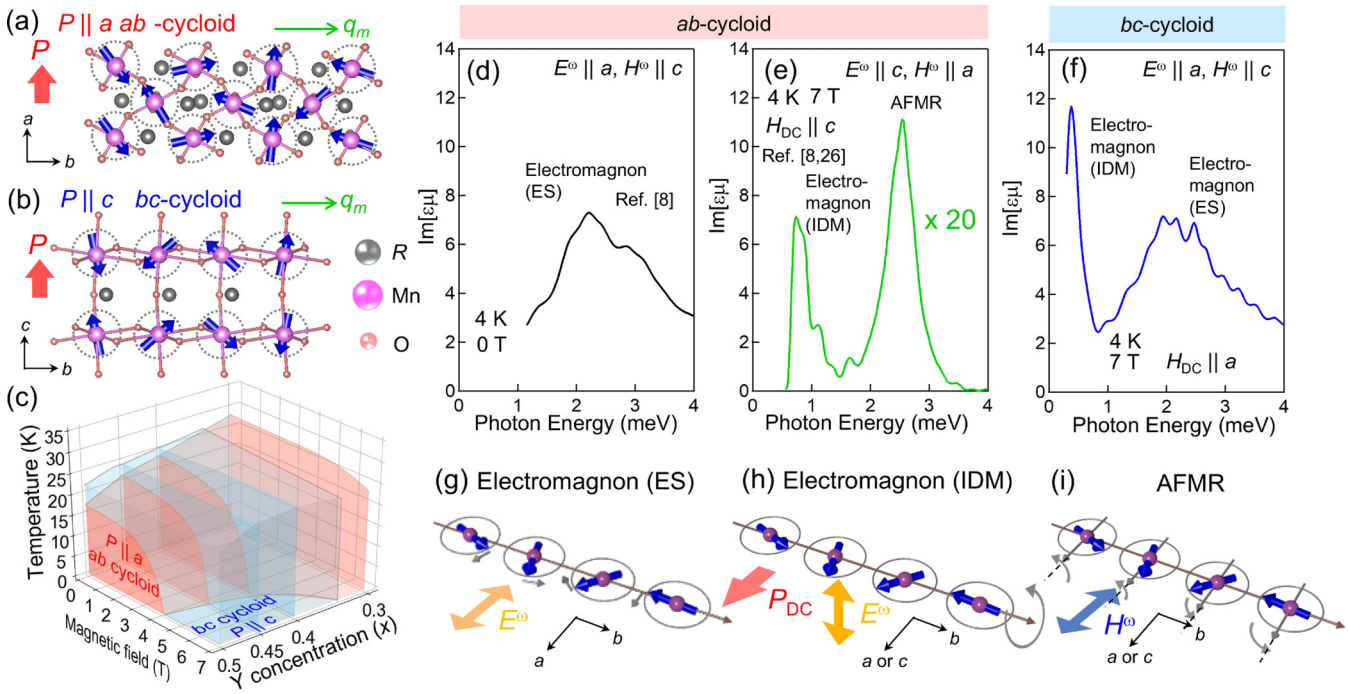

FIG. 2. Spin structures of perovskite manganite $RMnO_3$ (*R*: rare earth) in (a) the *ab*- and (b) *bc*-cycloid phases. (c) Magnetic phase diagram of $Eu_{1-x}Y_xMnO_3$. Phase diagrams of $x = 0.3$ and $x = 0.5$ are determined from polarization-temperature and magnetization-temperature curves, respectively. Data for $x = 0.4$ and $x = 0.45$ are taken from Refs. [19,20], respectively. The magnetic field is parallel to the *a* axis. The terahertz spectra of magnetic resonances in the *ab*-cycloid phase ($x = 0.45$) for (d) $\boldsymbol{E}^\omega \parallel a$ and $\boldsymbol{H}^\omega \parallel c$ at 4 K and 0 T and (e) $\boldsymbol{E}^\omega \parallel c$ and $\boldsymbol{H}^\omega \parallel a$ at 4 K in the magnetic field along the *c* axis [8,21]. (f) That in *bc*-cycloid phase ($x = 0.45$) for $\boldsymbol{E}^\omega \parallel a$ and $\boldsymbol{H}^\omega \parallel c$ at 4 K in the magnetic field along the *a* axis. Schematics of spin dynamics of (g) electromagnons driven by the ES mechanism, (h) electromagnons driven by the IDM mechanism, and (i) AFMR.

0.4, 0.45, 0.5). By using the terahertz time-domain polarimetry in the magnetic field, we demonstrate these effects in three distinct experimental configurations: NDD for the *ab* cycloid ($\boldsymbol{P} \parallel a$ and $\boldsymbol{M} \parallel c$) and for the *bc* cycloid ($\boldsymbol{P} \parallel c$ and $\boldsymbol{M} \parallel a$) and GB for the *ab* cycloid ($\boldsymbol{P} \parallel a$ and $\boldsymbol{M} \parallel a$). The emergence of these nonreciprocal optical responses indicates the resonantly enhanced dynamical ME coupling of the magnetic excitations. The Y concentration x dependence of the NDD is roughly scaled by the relevant coupled order parameter $\boldsymbol{P} \times \boldsymbol{M}$. In contrast, the magnitude of GB shows a clear deviation from its relevant coupled order parameter $\boldsymbol{P} \cdot \boldsymbol{M}$. We found that the GB is remarkably enhanced around the phase boundary between the *ab* cycloid and A-type antiferromagnetic phase.

II. EXPERIMENT

Single crystals of $Eu_{1-x}Y_xMnO_3$, with $x = 0.3$, 0.4, 0.45, 0.5, were prepared by the high-pressure floating-zone method. The samples were cut into plates with a thickness of 300–1000 μm for the optical measurements. In order to measure the optical ME effects, we performed terahertz time-domain polarimetry. A pulse laser with a center wavelength of 800 nm and a pulse duration of 100 fs was used to generate and detect terahertz pulses through the photoconductive antennas. By virtue of terahertz time-domain spectroscopy, complex optical constants of materials in the form of the refractive index or effective dielectric constants $\epsilon\mu$ can be directly obtained without resorting to Kramers-Kronig transformation [26]. The external magnetic field was applied perpendicular to the light propagation direction (Voigt configuration) for all three experiments (see Secs. IV A, IV B, and IV C). The wire grid polarizers before and after the sample were used for the polarimetry measurement of GB [11,27]. The detailed procedure of the polarization analysis is described elsewhere [28]. The single ferroelectric domain was formed by the electric field cooling from the paraelectric phase. The typical strength of the electric field, 1000 V/cm, is larger than that used in the early work with $x = 0.45$ (400 V/cm) [20]. No electric field was applied during the optical measurement.

III. OPTICAL PROPERTIES

A. Collective spin excitations

In perovskite manganite, three distinct collective spin excitations appear in the terahertz region: the electromagnons driven by the IDM mechanism and by the exchange-striction (ES) mechanism and the antiferromagnetic resonance [AFMR; Figs. 2(d)–2(i)]. The electromagnon driven by the IDM mechanism is the Nambu-Goldstone mode of the spin cycloid; the rotational oscillation of the spin plane gives rise to the electric transition dipole perpendicular to $\boldsymbol{P}$ [Fig. 2(h)] [17]. For the *ab* and *bc* cycloids, therefore, the electromagnon driven by the IDM mechanism has an electric transition dipole along the *c* axis [Fig. 2(e)] and along the *a* axis [Fig. 2(f)], respectively. The resonance energy of this electromagnon is dominated by the magnetic anisotropy and Zeeman energy, so that the resonance peak is located below 1 meV. On the other hand, the noncollinear spin orders in a particular lattice symmetry give rise to the electromagnon driven by the ES mechanism [Fig. 2(g)]. In RMnO$_3$ with *Pbnm* symmetry, the electric field of light along the *a* axis ($\boldsymbol{E}^\omega \parallel a$) generates the ES-driven electromagnon regardless of the spin-cycloidal plane [Figs. 2(d) and 2(f)] [21,26,29]. This electromagnon induces the antiphase oscillation of neighboring spins, which has been ascribed to the phason of the spin cycloid at the zone edge of the Brillouin zone ($q = \pi$) [30]. Thus, the electromagnon driven by the ES mechanism is always gapped; this zone-edge mode is located around 8 meV for $x = 0.45$ [21]. In RMnO$_3$, the ES-driven electromagnon has two peaks with intrinsically broad spectral widths. The lower-lying peak around 2 meV has been ascribed to the ES-driven electromagnon with $q = \pi - 2q_m$ [25,31] [Figs. 2(d) and 2(f)]. The spin cycloid shows the conventional AFMR with in-plane magnetic activity; the *ab* cycloid has AFMR with $\boldsymbol{H}^\omega \parallel a$ [Figs. 2(e) and 2(i)] [32].

B. General remarks on optical ME effects

The linear ME effects are described by the bilinear coupling between the electric field and the magnetic field in free energy as $F = \alpha_{ij}E_iH_j$ $(i, j = x, y, z)$, where α_{ij} represents the ME tensor [33]. Simultaneous breaking of time-reversal and space-inversion symmetries gives rise to these linear ME effects. Thus, the materials with both $\boldsymbol{P}$ and $\boldsymbol{M}$ always show the linear ME effects. The dynamical ME effects at frequency ω, $\alpha_{ij}(\omega)$, induce the optical ME effects with nonreciprocity. The diagonal and off-diagonal elements of $\alpha_{ij}(\omega)$ are responsible for the different optical ME effects, GB and NDD, respectively.

For example, the mutually orthogonal $\boldsymbol{P} \parallel x$ and $\boldsymbol{M} \parallel y$ [Fig. 1(a)] induce the off-diagonal ME coupling as follows:

$$\alpha(\omega) = \begin{bmatrix} 0 & \alpha_{xy}(\omega) & 0 \\ \alpha_{yx}(\omega) & 0 & 0 \\ 0 & 0 & 0 \end{bmatrix}. \tag{1}$$

The toroidal moment along the *z* axis also gives rise to similar ME coupling [34]. These off-diagonal ME couplings cause the NDD for the light propagating along the *z* axis. The resulting refractive index is described as $\tilde{N}_i(\omega) = \tilde{N}_i^{\mathrm{o}}(\omega) + \mathrm{sgn}(k^\omega)\alpha_{ij}(\omega)$ for light polarization $E^\omega \parallel i$ and $H^\omega \parallel j$, where $\tilde{N}_i$ is the total complex refractive index and $\tilde{N}_i^{\mathrm{o}}$ is the ordinary term [8,13]. In Secs. IV A and IV B, we demonstrate the NDD in two different phases: *ab*-cycloid ($\boldsymbol{P} \parallel a$ and $\boldsymbol{M} \parallel c$) and *bc*-cycloid ($\boldsymbol{P} \parallel c$ and $\boldsymbol{M} \parallel a$) phases.

The mutually parallel $\boldsymbol{P}$ and $\boldsymbol{M}$ [Fig. 1(b)] induce the diagonal elements of $\alpha(\omega)$, described as

$$\alpha(\omega) = \begin{bmatrix} \alpha_{xx}(\omega) & 0 & 0 \\ 0 & \alpha_{yy}(\omega) & 0 \\ 0 & 0 & \alpha_{zz}(\omega) \end{bmatrix}. \tag{2}$$

This diagonal ME coupling also emerges in the axionic electrodynamics in topological matter [35–37], as well as in the ME monopole [38,39]. The diagonal ME coupling gives rise to the GB observed as the nonreciprocal polarization rotation [14,40] [Fig. 1(b)] because the induced electric polarization by H^ω is always perpendicular to E^ω as $E^\omega \perp \alpha_{ii}(\omega)H^\omega$. In the transmission geometry, the magnitude of the optical rotation depends on the ME coupling $\alpha_{ii}(\omega)$, dielectric

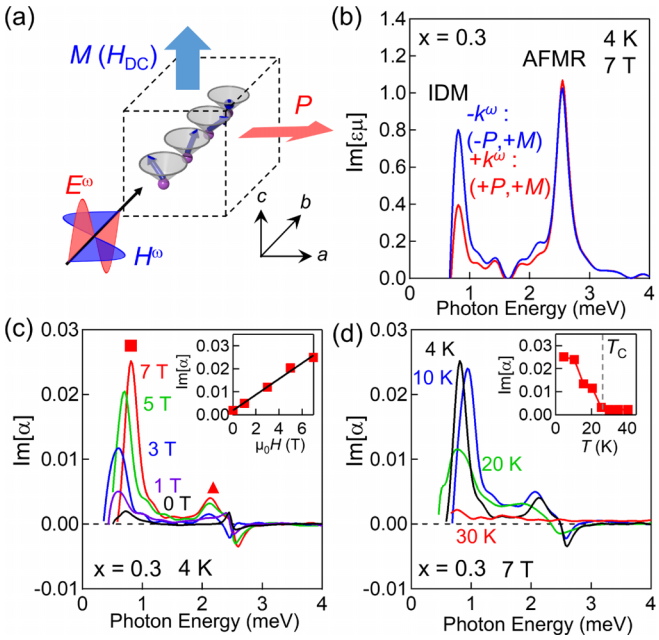

FIG. 3. (a) Schematic of NDD in the *ab*-cycloid phase. The *ab* cycloid gives rise to the spontaneous $\boldsymbol{P}$ along the a axis, and $\boldsymbol{M}$ along the c axis is induced by the external magnetic field. The light propagation vector $\boldsymbol{k}^{\omega}$ is parallel to the b axis. (b) Im[$\epsilon\mu$] spectra for $\boldsymbol{E}^{\omega} \parallel c$ and $\boldsymbol{H}^{\omega} \parallel a$ ($x = 0.3$). The red and blue lines represent the spectra for $(+P, +M)$ and $(-P, +M)$, respectively. (c) Magnetic field dependence of Im[α_{ca}] spectra at 4 K. The inset shows the peak magnitude of Im[α_{ca}] for electromagnons driven by the IDM mechanism at 0.9 meV. (d) The Im[α_{ca}] spectra for various temperatures at 7 T. The inset shows the temperature dependence of the peak magnitude of Im[α_{ca}] for the electromagnons driven by the IDM mechanism.

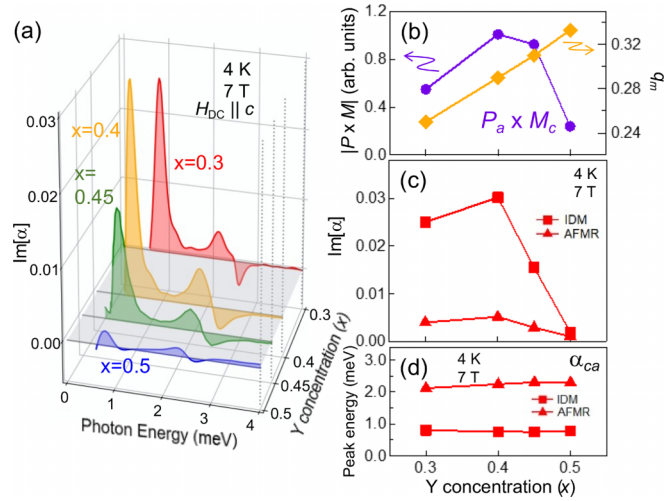

FIG. 4. (a) The ME spectra (Im[α_{ca}]) for $x = 0.3$, 0.4, 0.45, and 0.5. (b) The x dependence of the absolute value of the coupled order parameter $|\boldsymbol{P} \times \boldsymbol{M}|$ [19,20,41] (purple circles) and magnetic modulation vector q_m [19,22] (yellow diamonds). (c) The peak magnitude and (d) the peak energy of Im[α_{ca}] spectra for electromagnons driven by the IDM mechanism (squares) and AFMR (triangles).

spectra, and sample thickness. From terahertz polarimetry, the diagonal ME spectra $\alpha_{ii}(\omega)$ can be calculated with a direct procedure [28]. The GB for the *ab* cycloid is demonstrated in this work (Sec. IV C).

Since the optical ME effects are odd for the reversal of $\boldsymbol{P}$, $\boldsymbol{M}$, or $\boldsymbol{k}^{\omega}$, the signs of NDD and GB are expressed by the signs of $\boldsymbol{k}^{\omega} \cdot (\boldsymbol{P} \times \boldsymbol{M})$ and $k^{\omega}(\boldsymbol{P} \cdot \boldsymbol{M})$, respectively. Accordingly, the reversal of $\boldsymbol{k}^{\omega}$ is equivalent to the reversal of either $\boldsymbol{P}$ or $\boldsymbol{M}$. In this paper, the optical spectra of NDD and GB are denoted as $\pm k^{\omega}$, although these spectra were obtained by the reversal of $\boldsymbol{P}$.

IV. RESULTS

A. NDD for the *ab* cycloid

First, we show the NDD in the *ab*-cycloid phase ($\boldsymbol{P} \parallel a$) for $x = 0.3$. The magnetic field along the c axis induces the conelike cycloidal spins (transverse conical structure) shown in Fig. 3(a), giving rise to the NDD for the incident light with $\boldsymbol{k}^{\omega} \parallel \boldsymbol{P} \times \boldsymbol{M} \parallel b$. Figure 3(b) shows the imaginary part of the $\epsilon\mu$ spectra (Im[$\epsilon\mu$]) for $\boldsymbol{E}^{\omega} \parallel c$ and $\boldsymbol{H}^{\omega} \parallel a$ at 7 T. In the electromagnon driven by the IDM mechanism (0.9 meV; see also the mode characteristics in Fig. 2), a significant change in optical absorption is observed with the reversal of $\boldsymbol{P}$, indicating the resonantly enhanced NDD on the electromagnon. On the other hand, the AFMR at 2.5 meV shows a tiny NDD. These results are consistent with previous results for $x = 0.45$ [8]. The ME spectra α_{ca} are calculated from the refractive index as $\alpha_{ca} = \frac{1}{2}[\tilde{N}_c(+k^{\omega}) - \tilde{N}_c(-k^{\omega})]$. The imaginary part of α_{ca} (Im[α_{ca}]) [Fig. 3(c)], which represents the nonreciprocity of optical absorption, shows a clear peak structure in the electromagnon resonance at 0.9 meV, while a dispersive structure is observed in the AFMR at 2.5 meV. The peak magnitude of NDD (Im[α_{ca}]) is almost proportional to the magnetic field [inset of Fig. 3(c)], which is consistent with the increase in the relevant bilinearly coupled order parameter $\boldsymbol{P} \times \boldsymbol{M}$; $\boldsymbol{M}$ is proportional to the magnetic field, while $\boldsymbol{P}$ is almost intact below 7 T. Note that although a few tiny structures are discerned at 0 T [black line in Fig. 3(c)], these signals can be ascribed to experimental error. Figure 3(d) shows the temperature dependence of the ME spectra at 7 T. The NDD decreases with increasing temperature and disappears above $T_C = 26$ K. This clear correlation with the phase transition manifests the essential role of $\boldsymbol{P}$ arising from the *ab* cycloid for the NDD.

Next, we examine the x dependence of the NDD in the *ab*-cycloid phase. Figure 4(a) shows the NDD spectra (Im[α_{ca}]) for $x = 0.3$, 0.4, 0.45, and 0.5. All compositions show a similar spectral shape: a peak structure at 0.9 meV (electromagnon) and a dispersive structure at 2.5 meV (AFMR) [Fig. 4(d)]. In contrast, the magnitude of the NDD shows strong composition dependence [Figs. 4(a) and 4(c)]. The NDD for the electromagnon and AFMR is enhanced around $x = 0.4$; the peak magnitude for $x = 0.4$ is 15 times larger than that for $x = 0.5$. The coupled order parameter $\boldsymbol{P} \times \boldsymbol{M}$ also shows the domelike shape with a peak at $x = 0.4$ [Fig. 4(b)]. These results indicate that the coupled order parameter $\boldsymbol{P} \times \boldsymbol{M}$ is, even for the composition dependence, the dominant scaling factor for the NDD. This behavior is reasonable because the electromagnon driven by the IDM mechanism, which is the rotation mode of the spin-cycloid

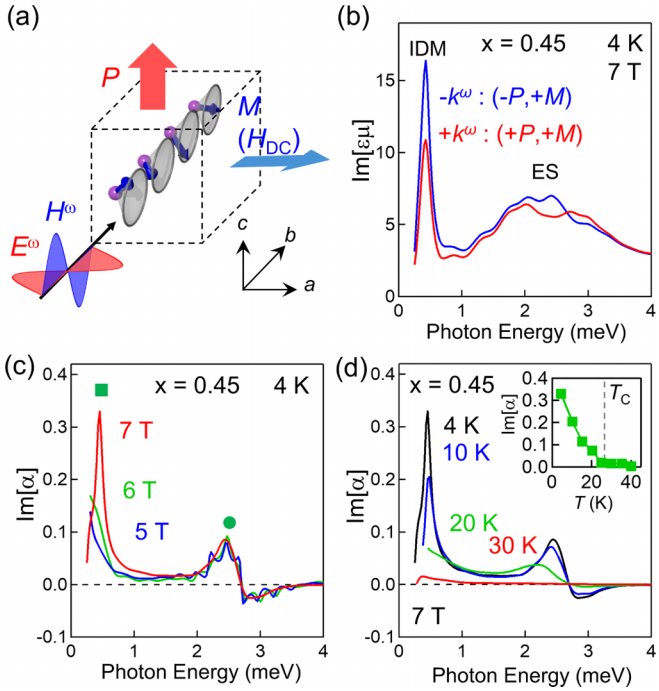

FIG. 5. (a) Schematic of NDD in the *bc*-cycloid phase. Here the *bc* cycloid is stabilized only in the magnetic field at the lowest temperature [see the phase diagram; Fig. 2(c)]. The *bc* cycloid gives rise to the spontaneous $\boldsymbol{P}$ along the c axis, and the external magnetic field induces $\boldsymbol{M}$ along the a axis. The light propagates along the b axis. (b) The electromagnon spectra for $\boldsymbol{E}^\omega \parallel a$ and $\boldsymbol{H}^\omega \parallel c$ ($x = 0.45$). The red and blue lines represent the spectra for $(+P, +M)$ and $(-P, +M)$, respectively. (c) The magnetic field dependence of Im[α_{ac}] spectra at 4 K. (d) The temperature dependence of NDD at 7 T. The inset shows the temperature dependence of peak magnitude.

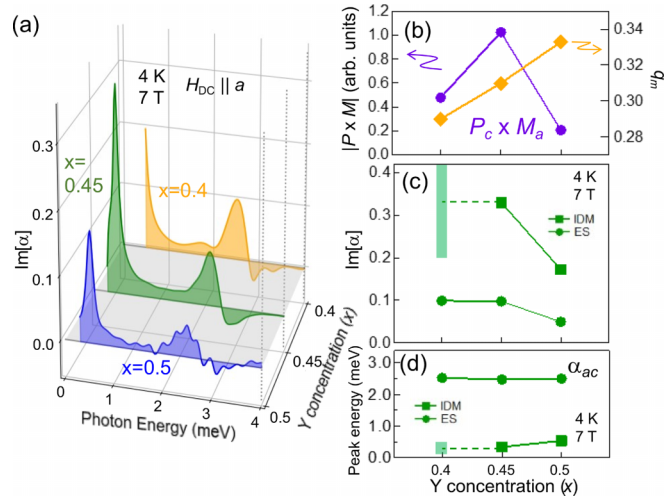

FIG. 6. (a) The ME spectra (Im[α_{ac}]) for $x = 0.4$, 0.45, and 0.5. (b) The x dependence of $|\boldsymbol{P} \times \boldsymbol{M}|$ [19,20] (purple circles) and magnetic modulation vector q_m [19,22] (yellow diamonds). (c) The peak magnitude and (d) the peak energy of Im[α_{ac}] for electromagnons driven by IDM (squares) and by the ES mechanism (circles). The estimated range of magnitude and energy of NDD for $x = 0.4$ is indicated in light green in (c) and (d).

plane [Fig. 2(h)], can be viewed as the rotatory oscillation of $\boldsymbol{P}$ and $\boldsymbol{M}$.

B. NDD for the *bc* cycloid

In $Eu_{1-x}Y_xMnO_3$, the spin cycloid flops from the *ab* to the *bc* plane in the magnetic field along the a axis [see Fig. 2(c)], resulting in the flop of $\boldsymbol{P}$ from the a axis to the c axis (4.2 T for $x = 0.45$). The conical *bc* cycloid with $\boldsymbol{P} \parallel c$ and $\boldsymbol{M} \parallel a$ allows the NDD for $\boldsymbol{k}^\omega \parallel b$ [Fig. 5(a)]. In the *bc*-cycloid phase, both electromagnons driven by the IDM and ES mechanisms have the same polarization, $\boldsymbol{E}^\omega \parallel a$ [see Fig. 2(f)]. The NDD for $x = 0.45$ is summarized in Fig. 5. The peak magnitude of the electromagnon driven by the IDM mechanism at 0.4 meV exceeds that in the *ab*-cycloid phase by 10 times (see Sec. IV A). This result is consistent with previous work on the *bc* cycloid in $Gd_{0.5}Tb_{0.5}MnO_3$ [9], in which the enhancement of the electromagnon driven by the IDM mechanism was explained by the transfer of oscillator strength from that by the ES mechanism through strong mode-mode coupling. A large NDD is observed in the resonances of both electromagnons [Fig. 5(b)]. The nonreciprocity of optical absorption is as large as $\Delta\mathrm{Im}[\epsilon\mu] \sim 6$ for the electromagnon driven by the IDM mechanism (~0.4 meV), while it is relatively small for the electromagnon driven by the ES mechanism (~2.5 meV). The enhanced NDD for the *bc* cycloid is more clearly manifested in the ME spectra [Fig. 5(c)]; the peak magnitude of Im[α_{ac}] in the *bc*-cycloid phase [~0.33 at 7 T; Fig. 5(c)] is 13 times larger than that of Im[α_{ca}] in the *ab*-cycloid phase [~0.025 at 7 T; Fig. 3(c)]. Figure 5(d) shows the temperature dependence of Im[α_{ac}]. The magnitude of the ME resonance monotonically decreases towards $T_C = 24$ K (inset) and vanishes above T_C, which is consistent with the disappearance of $\boldsymbol{P}$. Figure 6(a) summarizes the ME spectra in the *bc*-cycloid phase for $x = 0.4$, 0.45, and 0.5. Here we exclude $x = 0.3$ because the *ab*-cycloid phase remains even at 7 T [Fig. 2(c)]. Regardless of the Y concentration, the electromagnon shows an enhanced NDD in the *bc*-cycloid phase compared to the *ab*-cycloid phase [see Fig. 4(a)]. For $x = 0.4$, the peak of the lower-lying electromagnon cannot be detected because of the limitation of the sample size. The electromagnon driven by the ES mechanism [~2.5 meV; circles in Fig. 6(c)] shows comparable ME coupling (Im[α_{ac}]) for $x = 0.4$ and $x = 0.45$, while a reduction in the NDD is observed for $x = 0.5$. The maximum NDD for the IDM mode appears to be around $x = 0.4$–0.45 [squares in Fig. 6(c)]. In the *bc*-cycloid phase, the bilinearly coupled order parameters $\boldsymbol{P} \times \boldsymbol{M}$ [Fig. 6(b)] have a peak around $x = 0.45$, similar to that in the *ab*-cycloid phase [Fig. 4(b)]. Although the overall trend of these x dependences is not clear, the reduction in both $\boldsymbol{P} \times \boldsymbol{M}$ and the NDD (Im[α_{ac}]) at $x = 0.5$ [Fig. 6(c)] may imply the correlation between them.

C. GB for the *ab* cycloid

In the *ab*-cycloid phase, the magnetic field along the a axis induces $\boldsymbol{M} \parallel \boldsymbol{P} \parallel a$, giving rise to the GB [40] [Figs. 1(b) and 7(a)]. As shown in Fig. 2(c), this *ab* cycloid remains in the lower magnetic field below the spin-flop transition. Figure 7(b) shows the spectra of magnetic resonances for $x = 0.3$; the electromagnon resonance ($\boldsymbol{E}^\omega \parallel a$, red line)

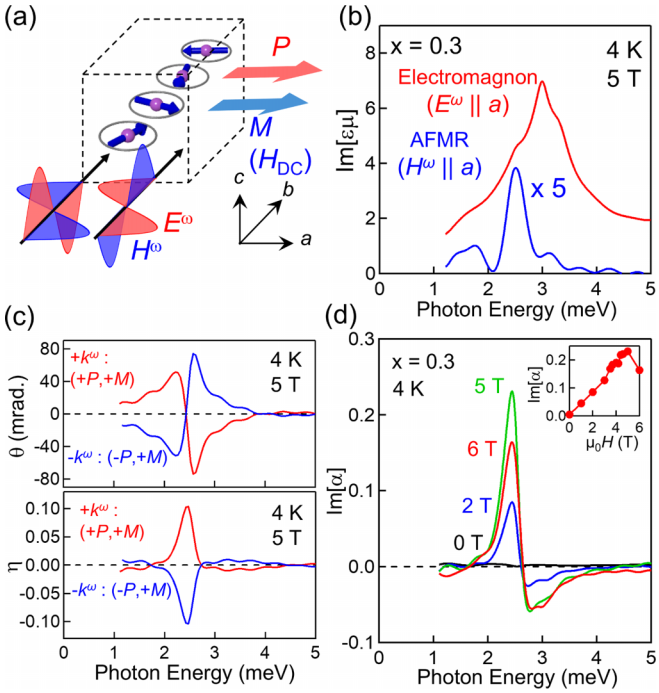

FIG. 7. (a) Schematic of GB in the *ab*-cycloid phase. The *ab* cycloid gives rise to $\boldsymbol{P}$ along the *a* axis, and the external magnetic field induces $\boldsymbol{M}$ along the *a* axis. The light propagates along the *b* axis. (b) Im[$\epsilon\mu$] spectra for $\boldsymbol{E}^\omega \parallel a$ and $\boldsymbol{H}^\omega \parallel c$ (red line, electromagnons) and for $\boldsymbol{E}^\omega \parallel c$ and $\boldsymbol{H}^\omega \parallel a$ (blue line, AFMR) for $x = 0.3$. (c) The spectra of rotation angle θ and ellipticity η at 4 K and 5 T. The sample thickness is 370 μm, and the polarization of incident light is $\boldsymbol{E}^\omega \parallel c$ and $\boldsymbol{H}^\omega \parallel a$. (d) The magnetic field dependence of Im[α_{aa}] spectra at 4 K. The inset shows the magnetic field dependence of the peak magnitude of Im[α_{aa}].

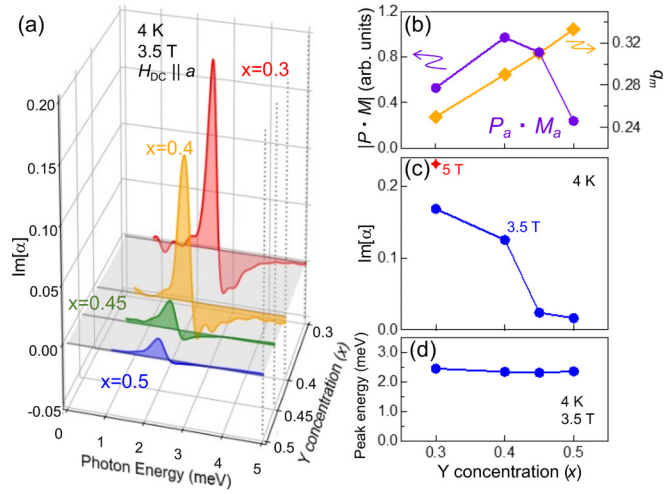

FIG. 8. (a) The ME spectra (Im[α_{aa}]) for each composition ($x =$ 0.3, 0.4, 0.45 [28], 0.5). (b) The x dependence of $|\boldsymbol{P} \cdot \boldsymbol{M}|$ [19,20] (purple circles) and the magnetic modulation vector q_m [19,22] (yellow diamonds). (c) The peak magnitude (blue circles for 3.5 T and red star for 5 T) and (d) the peak energy of Im[α_{aa}].

driven by the ES mechanism appears around 3.0 meV, and the AFMR ($\boldsymbol{H}^\omega \parallel a$, blue line) is observed at 2.5 meV. Figure 7(c) shows the optical rotation spectra, the rotation angle θ and ellipticity η, for the sample with a thickness of 370 μm. The dispersive structure in θ and peak structure in η show the sign change under the reversal of $\boldsymbol{P}$, indicating the emergence of GB. Im[α_{aa}] deduced from terahertz polarimetry shows a pronounced resonance [Fig. 7(d)] [28]. As we discuss later, the mode-mode coupling between the AFMR ($H^\omega \parallel a$) and the ES-driven electromagnon ($E^\omega \parallel a$) gives rise to the resonantly enhanced GB. Im[α_{aa}] increases with increasing magnetic field below 5 T [inset of Fig. 7(d)], while retaining the spectral shape. The decrease in Im[α_{aa}] above 5 T may be caused by the decrease in $\boldsymbol{P}$ near the transition to the *bc*-cycloid phase. Figure 8(a) summarizes the composition dependence of GB. For all the compositions, the asymmetric resonance peak appears around 2.5 meV, while the magnitude of the resonance strongly depends on x [Figs. 8(c) and 8(d)]. The striking feature is that the magnitude is significantly enhanced at $x = 0.3$, 0.4 [Fig. 8(c)], whereas the corresponding order parameter $\boldsymbol{P} \cdot \boldsymbol{M}$ has a domelike shape [Fig. 8(b)] with the peak around $x = 0.4$. The peak of Im[α_{aa}] for $x = 0.3$ ($\sim$0.17) is 11 times larger than that for $x = 0.5$ ($\sim$0.015) at 3.5 T [blue line in Fig. 8(c)]. A further increase of Im[α_{aa}] is observed for $x = 0.3$ in the larger magnetic field; Im[α_{aa}] approaches 0.23 at 5 T [red diamond in Fig. 8(c)].

V. DISCUSSION

The optical ME effects are interpreted as the interference between electric and magnetic transition dipoles. The optical process of the NDD and GB is described as follows [42]:

$$\alpha_{ij}(\omega) \propto \sum_n \frac{\langle 0|\,\Delta p_i\,|n\rangle\,\langle n|\,\Delta m_j\,|0\rangle}{\omega_{n0} - \omega - i\delta} \quad (i, j = x, y, z). \tag{3}$$

$\langle 0|\,\Delta p\,|n\rangle$ and $\langle n|\,\Delta m\,|0\rangle$ are the electric and magnetic transition dipole amplitudes between the ground and excited states, respectively. δ is a phenomenological damping factor. In both the *ab*- and *bc*-cycloid phases, the electromagnon driven by the IDM mechanism always has both electric and magnetic transition dipoles, resulting in the resonance in α_{ca} (Sec. IV A) and α_{ac} (Sec. IV B) at 0.9 meV, respectively. The dynamical ME coupling $\alpha_{aa}(\omega)$, which is responsible for GB in the *ab*-cycloid phase, requires the interference of the electric transition dipole and the magnetic one along the *a* axis. The electromagnon driven by the ES mechanism has the electric transition dipole along the *a* axis, while the AFMR has the magnetic one along the *a* axis. It has been concluded that the mode-mode coupling between the AFMR and ES-driven electromagnon is essentially important for the GB [28].

The aforementioned different mode characters of electromagnons provide insight into the x dependence of the NDD and GB. For the NDD, the x dependence of Im[α] is roughly consistent with that of the relevant coupled order parameter [$\boldsymbol{P} \times \boldsymbol{M}$; Fig. 4(c)]. The IDM mechanism gives rise to both spontaneous $\boldsymbol{P}$ and the electromagnon producing the NDD, so that the magnitude of the NDD on the electromagnon shows a correlation with $\boldsymbol{P}$, as mentioned in Sec. IV A. In contrast, the x dependence of GB shows a large deviation from the relevant order parameters ($\boldsymbol{P} \cdot \boldsymbol{M}$); Im[$\alpha$] shows a monotonic

increase in intensity with decreasing x [Fig. 8(c)], while $\boldsymbol{P} \cdot \boldsymbol{M}$ shows a domelike shape [Fig. 8(b)]. A possible cause of this x dependence of GB is the change in the strength of mode-mode coupling between the electromagnon driven by the ES mechanism and the AFMR. In general, the mode-mode coupling originates from the anharmonic term for the potential surface of elementary excitations, so the enhancement of GB indicates that anharmonicity of these magnetic excitations significantly develops around $x = 0.3$. The anharmonicity of elementary excitations is often pronounced near a phase transition. In fact, $x = 0.3$ is close to the phase boundary to the weakly canted A-type antiferromagnetic phase, which becomes the ground state around $x = 0.2$ [19,41]. Therefore, in addition to the relevant order parameters, the large anharmonicity, or, equivalently, the mode-mode coupling strength, for electromagnons and AFMR is also an important factor for the enhancement of optical ME effects. We note that the enhanced NDD in the bc-cycloid phase is also affected by the mode-mode coupling, as reported for $Gb_{0.5}Tb_{0.5}MnO_3$ [9], which is also located near the phase boundary.

The diagonal ME coupling inducing GB is significantly enhanced for $x = 0.3$, as shown in Fig. 8(c); the magnitude of the dynamical ME coefficient $\mathrm{Im}[\alpha_{aa}]$ approaches ~0.23 (= 770 ps/m) at 5 T. Here the ME coefficient in SI units is obtained by dividing by the velocity of light c. This value is larger than the previously observed GB: $\mathrm{Im}[\alpha] \sim 2.2 \times 10^{-4}$ (= 0.73 ps/m) in Cr_2O_3 [12], $\mathrm{Im}[\alpha] \sim 0.045$ (= 150 ps/m) in $(Fe, Zn)_2Mo_3O_8$ [43], and $\mathrm{Im}[\alpha] \sim 0.05$ (= 165 ps/m) in $Cu(Fe, Ga)O_2$ [11]. The observed large peak magnitude can be compared with the static (DC) linear diagonal ME coefficient: $\alpha \sim 1.2$–1.5×10^{-3} (= 4.0–5.0 ps/m) in Cr_2O_3 [44], $\alpha \sim 0.090$ (= 300 ps/m) in $TbPO_4$ [45], and $\alpha \sim 0.043$ (= 142 ps/m) in $(Fe, Zn)_2Mo_3O_8$ [46]. Recently, the quantized ME coupling was discussed for topological materials: $\alpha = \frac{e^2\theta_{\mathrm{topo}}}{4\pi^2\hbar c} \sim 7.3 \times 10^{-3}$ (= 24 ps/m), where $h = 2\pi\hbar$ is Planck's constant, $e > 0$ is the magnitude of the electron's charge, and $\theta_{\mathrm{topo}} = \pi$ for quantized states [47]. The large diagonal ME coefficient observed in the present study indicates that ME multiferroics with electromagnons realize the giant dynamical ME coupling and probably the strong static ME coupling among various classes of materials.

VI. CONCLUSION

We systematically investigated the optical ME effects including the NDD and GB in the magnetic excitations in $Eu_{1-x}Y_xMnO_3$ ($x = 0.3$, 0.4, 0.45, 0.5) in terms of terahertz time-domain polarimetry. The magnitude of ME spectra strongly depends on x, while the spectral shape and peak energy show little x dependence for each optical ME effect. The enhanced NDD is observed on the electromagnon driven by the IDM mechanism in both ab- and bc-cycloid phases. The composition dependence of NDD roughly scales with the bilinearly coupled order parameters ($\boldsymbol{P} \times \boldsymbol{M}$). In contrast, the electromagnon driven by the ES mechanism and AFMR cooperatively produce the enhanced GB in the ab-cycloid phase. The x dependence of GB shows a large deviation from the relevant coupled order parameter ($\boldsymbol{P} \cdot \boldsymbol{M}$). The GB is dramatically enhanced around $x = 0.3$, located near the phase boundary of cycloidal and weakly canted antiferromagnetic phases. The peak magnitude of GB for $x = 0.3$ approaches $\mathrm{Im}[\alpha_{aa}] \sim 0.23$ (= 770 ps/m), which is the largest class of diagonal ME coupling known so far. Our results provide insight into the enhancement of the optical ME effect on the electromagnon resonance, potentially leading to nonreciprocal terahertz devices. Recently, ME coupling has attracted increasing attention in terms of dynamical axion quasiparticles in condensed matter, especially in the energy range of meV [48]. The enhanced ME coupling of the electromagnon could be a candidate for dynamical axion phenomena.

ACKNOWLEDGMENTS

This work has been supported by the Japan Science and Technology Agency through Grants No. JPMJPR1423 and No. JPMJCR16F1 and by Japan Society for the Promotion of Science KAKENHI (Grants No. 17K19050 and No. 17H04845).

[1] Y. Tokura, S. Shinichiro, and N. Nagaosa, Rep. Prog. Phys. **77**, 076501 (2014).
[2] S. W. Cheong and M. Mostovoy, Nat. Mater. **6**, 13 (2007).
[3] F. Matsukura, Y. Tokura, and H. Ohno, Nat. Nanotechnol. **10**, 209 (2015).
[4] T. Kimura, T. Goto, H. Shintani, K. Ishizuka, T. Arima, and Y. Tokura, Nature (London) **426**, 55 (2003).
[5] Y. Tokunaga, Y. Taguchi, T. Arima, and Y. Tokura, Nat. Phys. **8**, 838 (2012).
[6] S. Manipatruni, D. E. Nikonov, and I. A. Young, Nat. Phys. **14**, 338 (2018).
[7] Y. Tokura and N. Nagaosa, Nat. Commun. **9**, 3740 (2018).
[8] Y. Takahashi, R. Shimano, Y. Kaneko, H. Murakawa, and Y. Tokura, Nat. Phys. **8**, 121 (2012).
[9] Y. Takahashi, Y. Yamasaki, and Y. Tokura, Phys. Rev. Lett. **111**, 037204 (2013).
[10] I. Kezsmarki, N. Kida, H. Murakawa, S. Bordacs, Y. Onose, and Y. Tokura, Phys. Rev. Lett. **106**, 057403 (2011).
[11] S. Iguchi, R. Masuda, S. Seki, Y. Tokura, and Y. Takahashi, Nat. Commun. **12**, 6674 (2021).
[12] B. B. Krichevtsov, V. V. Pavlov, R. V. Pisarev, and V. N. Gridnev, J. Phys.: Condens. Matter. **5**, 8233 (1993).
[13] T. Roth and G. L. J. A. Rikken, Phys. Rev. Lett. **88**, 063001 (2002).
[14] T. Roth and G. L. J. A. Rikken, Phys. Rev. Lett. **85**, 4478 (2000).
[15] H. Katsura, N. Nagaosa, and A. V. Balatsky, Phys. Rev. Lett. **95**, 057205 (2005).
[16] M. Mostovoy, Phys. Rev. Lett. **96**, 067601 (2006).
[17] H. Katsura, A. V. Balatsky, and N. Nagaosa, Phys. Rev. Lett. **98**, 027203 (2007).
[18] I. A. Sergienko and E. Dagotto, Phys. Rev. B **73**, 094434 (2006).
[19] Y. Yamasaki, S. Miyasaka, T. Goto, H. Sagayama, T. Arima, and Y. Tokura, Phys. Rev. B **76**, 184418 (2007).
[20] H. Murakawa, Y. Onose, F. Kagawa, S. Ishiwata, Y. Kaneko, and Y. Tokura, Phys. Rev. Lett. **101**, 197207 (2008).

[21] Y. Takahashi, Y. Yamasaki, N. Kida, Y. Kaneko, T. Arima, R. Shimano, and Y. Tokura, Phys. Rev. B **79**, 214431 (2009).
[22] S. Ishiwata, Y. Kaneko, Y. Tokunaga, Y. Taguchi, T. H. Arima, and Y. Tokura, Phys. Rev. B **81**, 100411(R) (2010).
[23] J. S. Lee, N. Kida, S. Miyahara, Y. Takahashi, Y. Yamasaki, R. Shimano, N. Furukawa, and Y. Tokura, Phys. Rev. B **79**, 180403(R) (2009).
[24] M. Mochizuki and N. Furukawa, Phys. Rev. B **80**, 134416 (2009).
[25] M. Mochizuki, N. Furukawa, and N. Nagaosa, Phys. Rev. Lett. **104**, 177206 (2010).
[26] N. Kida, Y. Ikebe, Y. Takahashi, J. P. He, Y. Kaneko, Y. Yamasaki, R. Shimano, T. Arima, N. Nagaosa, and Y. Tokura, Phys. Rev. B **78**, 104414 (2008).
[27] R. Masuda, Y. Kaneko, Y. Tokura, and Y. Takahashi, Science **372**, 496 (2021).
[28] M. Ogino, Y. Kaneko, Y. Tokura, and Y. Takahashi, Phys. Rev. Res. **2**, 023345 (2020).
[29] A. Pimenov, A. A. Mukhin, V. Yu. Ivanov, V. D. Travkin, A. M. Balbashov, and A. Loidl, Nat. Phys. **2**, 97 (2006).
[30] R. Valdés Aguilar, M. Mostovoy, A. B. Sushkov, C. L. Zhang, Y. J. Choi, S. W. Cheong, and H. D. Drew, Phys. Rev. Lett. **102**, 047203 (2009).
[31] M. P. V. Stenberg and R. de Sousa, Phys. Rev. B **80**, 094419 (2009).
[32] D. Senff, N. Aliouane, D. N. Argyriou, A. Hiess, L. P. Regnault, P. Link, K. Hradil, Y. Sidis, and M. Braden, J. Phys.: Condens. Matter **20**, 434212 (2008).
[33] L. Landau and E. Lifshitz, *Electrodynamics of Continuous Media*, Course of Theoretical Physics (Pergamon, New York, 1975).
[34] N. A. Spaldin, M. Fiebig, and M. Mostovoy, J. Phys.: Condens. Matter **20**, 434203 (2008).
[35] F. W. Hehl, Y. N. Obukhov, J.-P. Rivera, and H. Schmid, Eur. Phys. J. B **71**, 321 (2009).
[36] X. L. Qi, T. L. Hughes, and S. C. Zhang, Phys. Rev. B **78**, 195424 (2008).
[37] F. Wilczek, Phys. Rev. Lett. **58**, 1799 (1987).
[38] D. Khomskii, Physics **2**, 20 (2009).
[39] N. A. Spaldin, M. Fechner, E. Bousquet, A. Balatsky, and L. Nordstrom, Phys. Rev. B **88**, 094429 (2013).
[40] R. M. Hornreich and S. Shtrikman, Phys. Rev. **171**, 1065 (1968).
[41] J. Hemberger, F. Schrettle, A. Pimenov, P. Lunkenheimer, V. Y. Ivanov, A. A. Mukhin, A. M. Balbashov, and A. Loidl, Phys. Rev. B **75**, 035118 (2007).
[42] S. Miyahara and N. Furukawa, Phys. Rev. B **89**, 195145 (2014).
[43] T. Kurumaji, Y. Takahashi, J. Fujioka, R. Masuda, H. Shishikura, S. Ishiwata, and Y. Tokura, Phys. Rev. Lett. **119**, 077206 (2017).
[44] H. Wiegelmann, A. G. M. Jansen, and P. Wyder, Ferroelectrics **162**, 141 (1994).
[45] G. T. Rado, J. M. Ferrari, and W. G. Maisch, Phys. Rev. B **29**, 4041 (1984).
[46] T. Kurumaji, S. Ishiwata, and Y. Tokura, Phys. Rev. X **5**, 031034 (2015).
[47] A. Sekine and K. Nomura, J. Appl. Phys. **129**, 141101 (2021).
[48] D. J. E. Marsh, K. C. Fong, E. W. Lentz, L. Smejkal, and M. N. Ali, Phys. Rev. Lett. **123**, 121601 (2019).